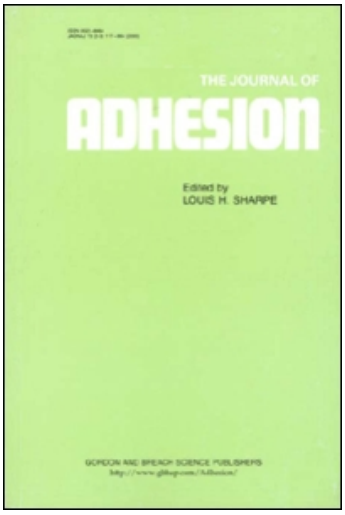

The Journal of Adhesion
Publication details, including instructions for authors and subscription information:
http://www.informaworld.com/smpp/title~content=t713453635

The Structure and Impurities of Hard DC Anodic Layers on AA6060 Aluminium Alloy

J. C. Walmsley[a]; C. J. Simensen[b]; A. Bjørgum[a]; F. Lapique[b]; K. Redford[bc]
[a] SINTEF Materials and Chemistry, Trondheim, Norway [b] SINTEF Materials and Chemistry, Oslo, Norway [c] Conpart AS, Skjetten, Norway

To cite this Article Walmsley, J. C. , Simensen, C. J. , Bjørgum, A. , Lapique, F. and Redford, K.(2008) 'The Structure and Impurities of Hard DC Anodic Layers on AA6060 Aluminium Alloy', The Journal of Adhesion, 84: 6, 543 — 561
To link to this Article: DOI: 10.1080/00218460802161590
URL: http://dx.doi.org/10.1080/00218460802161590

The Journal of Adhesion, 84:543–561, 2008

ISSN: 0021-8464 print/1545-5823 online
DOI: 10.1080/00218460802161590

Taylor & Francis
Taylor & Francis Group

The Structure and Impurities of Hard DC Anodic Layers on AA6060 Aluminium Alloy

J. C. Walmsley[1], C. J. Simensen[2], A. Bjørgum[1], F. Lapique[2], and K. Redford[2,3]
[1]SINTEF Materials and Chemistry, Trondheim, Norway
[2]SINTEF Materials and Chemistry, Oslo, Norway
[3]Conpart AS, Skjetten, Norway

Hard anodic layers produced under DC conditions in sulphuric acid on a commercial AA 6060 aluminium alloy have been characterised by electron microscopy and secondary ion mass spectroscopy (SIMS). Once exposed during anodising, α–Al(Fe, Mn)Si intermetallic particles start to corrode in the electrolyte. Partially corroded particles become trapped in the oxide, disturbing the local pore structure. This leads to pyramidal defects on the alloy surface and retention of isolated, unmodified fragments of alloy in the oxide. Sealing in boiling water left a low density, loosely attached surface layer of modified oxide that gave poor adhesion properties. The bulk oxide pore structure was modified by a uniform, fine network of bridges that extended down the barrier layer. Calibration of the SIMS sputtering rate allowed the concentration of alloying and impurity elements to be measured as a function of depth in the oxide and into the alloy.

Keywords: AA6060; Anodization; Intermetallic particles; SIMS; TEM

INTRODUCTION

Anodic oxide layers on aluminium alloys can provide surface hardness, corrosion protection, or act as a pretreatment for coated or bonded products. Sulphuric acid anodising (SAA) provides a high oxide growth rate and can be used when thicker layers are required. The corrosion resistance of the surface can be increased by immersion in boiling aqueous solution to "seal" the oxide pore structure. This can be

Received 22 October 2007; in final form 17 April 2008.
One of a collection of papers honoring John F. Watts, the recipient in February 2008 of *The Adhesion Society Award for Excellence in Adhesion Science, Sponsored by 3M*.
Address correspondence to J. C. Walmsley, SINTEF Materials and Chemistry, Høgskoleringen 5, NO-7465 Trondheim, Norway. E-mail: john.walmsley@sintef.no

particularly important in structural bonding or other applications where bare surfaces will remain exposed in service.

In earlier work, a range of AC and DC anodising conditions were assessed for their effectiveness as a pre-treatment for structural bonding applications of an AA6060 alloy using both phosphoric and sulphuric acid anodising. Basic properties such as anodic layer thickness, structure, density, and bond durability under accelerated exposure conditions were reported [1].

Here, we report further detail of the microstructural and chemical features observed in hard DC SAA oxide, paying particular attention to the behaviour of intermetallic particles, the composition of the oxide, and the effect of sealing. Electron microscopy was used to study the structure and discrete impurity content of the oxide and the effect of sealing on the surface and pore structure. Secondary ion mass spectroscopy (SIMS) was used to study the overall distribution of alloying and trace elements through the thickness of the oxide.

Commercial aluminium alloys contain secondary phases, solute atoms, and impurities. As the interface between the anodic oxide and substrate moves through the alloy during anodisation, these may be dissolved in the electrolyte, incorporated into the oxide, or, in the case of solutes, segregated to the oxide/alloy interface. This can influence the physical and chemical properties of the anodic layer and it is, therefore, of value to have a detailed understanding of the anodising response of a given commercial alloy. For example, Tsagaraki-Kaplanoglou *et al.* [2] have studied the influence of alloy type on alloy behaviour for heat treated and non-heat treated commercial AA5083 and AA6111 compared with pure aluminium in sulphuric acid baths. Under standard oxidising conditions, the AA6111 alloy was found to have a similar oxide growth rate to pure aluminium, and heat treatment of the alloy was found to improve the anodizing efficiency and kinetic slightly.

The behaviour of solute depends on thermodynamic considerations. Much of the understanding of these processes is based on the study of binary alloys [3–6]. According to Gibbs' free energy considerations, some elements are expected to oxidise and become incorporated into the alumina film, some are not initially oxidised, becoming enriched underneath the barrier layer, up to a critical enrichment over a typical depth of 1–2 nm, and others show semiconducting behaviour during oxidation and can cause the evolution of oxygen in the film during anodization [7].

Intermetallic particles and inclusions can be partially retained within the oxide. Shimizu *et al.* [8] found that Al_6Fe particles were incorporated into a SAA anodic layer on an Al-1.4 wt% Fe alloy, while

Al_3Fe particles were quite rapidly dissolved, leaving a modified local oxide composition. Shimizu *et al.* [9] have studied the modified oxide growing on exposed Al_3Fe particles at the surface of an Al-0.5% Fe alloy which was found to comprise amorpous Fe and Al oxide. For an AA7075 alloy in a sulphuric acid-oxalic acid electrolyte, Mukhopadhyay and Sharma [10] found that the influence of $Al_{12}(FeMn)_3Si$ particles on bath voltage with time and the uniformity of the film depended on the orientation of the particles with respect to the growth direction of the film and could be, at least partially, controlled by anodising in more aggressive sulphuric acid/oxalic acid/hydrochloric acid mixtures, which have a stronger tendency to dissolve the particles during anodisation. Fratila-Apachitei *et al.* [11] studied sulphuric acid hard anodised AlSi(Cu) alloys. For an Al-10 wt% Si alloy, Si particles were trapped in the oxide with subsequent oxidation of Si leading to the presence of oxygen filled voids. By contrast, $CuAl_2$ particles present in an Al-10 wt% Si-3 wt% Cu alloy were found to undergo complete oxidation during anodisation. Shimuzu *et al.* [12] described the influence of θ' matrix precipitates in an Al-1.86% Cu alloy. They found that the precipitates modify the formation process of the anodic film significantly by giving rise to film cracking and oxygen generation and this produced a highly flawed final film.

MATERIALS AND METHODS

AA6060 extrusions were provided by Hydro Aluminium (Raufoss, Norway) in the form of profiles that were originally 2 mm thick and 110 mm wide. The composition of the alloy is given in Table 1.

TABLE 1 Chemical Composition of the AA6060 Aluminium Alloy Investigated

Concentration (wt%)							
Al	Mg	Si	Mn	Fe	Ni	Cu	Zn
98.83	0.56	0.43	0.022	0.21	0.0023	0.0061	0.0069

Concentration (wtppm)								
B	Ti	V	Cr	Zr	Sn	Sb	Bi	Pb
13.5	134	59	30	20	2	7	7	16

Concentration (wtppm)								
Li	Na	Ca	P	Sr	Be	Cd	Co	Ga
0.4	11	4.1	7.4	0.4	1	0.4	4.6	156

AA6060 is a β″ hardened alloy that contains secondary intermetallic particles, mostly of the α–Al(Fe,Mn)Si phase. The extrusions were anodised in the industrialy T6 heat treated condition.

Anodising was carried out using the Computer Aided Pulse Plating (CAPP) software coupled to an AXA 25V/20A rectifier from Axel Åkerman A/S (Denmark). The amount of aluminium converted to oxide and the oxide layer thickness were determined gravimetrically by weighing control samples before and after anodising and after stripping the samples in chromic-phosphoric acid solution according to ASTM G1. Details of the SAA anodising conditions are given in Table 2. The initial alkaline etching step removed approximately 15 μm from the surface of the extrusions. Sealing was performed by boiling in distilled water.

For plan view scanning electron microscope (SEM) observation, small sections of approximately 1 cm square were examined directly. In order to get an impression of the internal structure of the anodised layer, back-thinned sections of the samples were cooled to liquid nitrogen temperature and then fractured by bending. This produced brittle fracture surfaces in cross-section geometry. SEM observations were made in a Hitachi (Tokyo, Japan) s-4300se field emission gun (FEG) SEM operating at 5 kV.

Samples studied in the transmission electron microscope (TEM) were prepared in cross-section geometry. TEM samples can be prepared very effectively by ultramicrotomy [8,13]. However, our relatively thick film samples were prepared by ion beam thinning. Pairs of 3 mm wide anodised strips were glued face-to-face and machined to a 3 mm diameter cylinder and slices of ∼400 μm thickness were cut. These were ground to a thickness of ∼100μm, dimple ground to a central thickness of ∼30 μm, and ion beam thinned to electron transparency using a Gatan (Pleasanton, California PIPS ion beam thinner. Samples were examined in a Philips (Hillsboro, USA). Oregon, USA, FEI CM30 TEM operated at 200 kV.

TABLE 2 Sulphuric Acid Anodising Conditions for AA 6060

	Alkaline etching 10 wt% NaOH, 60°C, 2 min followed by desmutting in HNO_3				
Pretreatment	wt% H_2SO_4	Current density (A/dm^2)	Time (min)	Temperature (°C)	Sealing
SAA	16	1.5	20	20	no
SAA sealed	16	1.5	20	20	distilled water

For SIMS, the anodised materials were analysed in a Cameca (Gennevilliers, France) IMS-4f SIMS using O^- as the sputtering agent. The energy of the ions was 12 keV. The diameter of the analysed area was approximately 50 μm. Isotopes analysed in the profiles reported here are ^{1}H, ^{24}Mg, ^{27}Al, ^{30}Si, ^{34}S, ^{40}Ca, ^{56}Fe, and ^{55}Mn. After the analysis the depth of the sputtered volume was determined with a Taylor-Hobson (Leicester, UK) Talysurf-10 profilometer to be 11 μm. The sputtering velocity was relatively slow, approximately 0.47 μm/hour. Procedures followed those established during earlier studies of aluminium alloys [14].

The concentration of the elements was determined by measuring the intensities (I_x) of the isotopes relative to the intensity of aluminium in the matrix (I_{Al}). The concentration is then:

$$C_x = K_{x/Al} \cdot J_x = K_{x/Al} \cdot \frac{f_{Al} \cdot I_x}{f_x \cdot I_{Al}} \cdot C_{Al}, \quad (1)$$

where C_{Al} is the concentration of aluminium in metal matrix (=98.83 at%), f is the abundance of the isotope ($f_{27Al} = 100\%$ etc.). J_x is the relative intensity of element x, and $K_{x/Al}$ is the sensitivity factor of element x. The sensitivity factors in the matrix were determined by averaging the measured intensities in the matrix of the different elements. Data were included from analyses of a number of samples anodised under different conditions, including several that are not described further here. The average concentration was, for most elements, determined by emission spectroscopy. It is well established that the sputtering velocity is dependent on the material sputtered, and is lower for materials with a high hardness. Thus, the sputtering velocity is lower in alumina than in aluminium. The measured intensities of an isotope x is correspondingly reduced in the oxide compared with the matrix:

$$I_{x,ox} = I_x v_{ox}/v_{Al} = I_x \theta, \quad (2)$$

where v_{ox} and v_{Al} are the sputtering velocities in the oxide and matrix, respectively, and θ is the relative sputtering speed of the oxide. If it is assumed that the sensitivity factors are the same in the oxide as in the matrix, except that all the intensities are correspondingly lower, the concentrations of an element x (isotope x) in the oxide can be determined by either comparing with the intensity of Al in the oxide or in the matrix. Thus:

$$C_{x,ox} = K_{x/Al} \cdot \frac{f_{Al} \cdot I_{x,ox}}{f_x \cdot I_{Al,ox}} \cdot C_{Al,ox} = K_{x/Al} \cdot \frac{f_{Al} \cdot I_{x,ox}}{\theta \cdot f_x \cdot I_{Al}} \cdot C_{Al}, \quad (3)$$

where the subscript x,ox in $I_{x,ox}$ refers to the intensity of an element x in the oxide, etc. The factor θ can be determined by measuring the

intensities of aluminium in the oxide and matrix, respectively, knowing the concentrations of aluminium in matrix and oxide:

$$\theta = \frac{C_{Al} \cdot I_{Al,ox}}{C_{Al,ox} \cdot I_{Al}}. \quad (4)$$

The concentration of aluminium is 98.83 at% in the matrix and approximately 40 at% in alumina. The intensity measurement using SIMS showed that $\theta \approx 0.36$–0.4. The change in the Al intensity going from the oxide into matrix was used to estimate the change in the sputtering rate.

RESULTS

SEM Observations

Figure 1A shows a low magnification view of a DC anodised Sample SAA. The loci of the underlying grain boundaries are visible in the surface topography of the oxide. This, and the scalloped morphology over the grain surfaces, reflects the surface topography produced by the original alkali etch. Figure 1B shows the pore structure at the surface of the oxide layer in finer detail. A number of large surface defects are visible. Figure 1C shows one of the latter in greater detail. Besides introducing an irregularity in the sample surface, the pore size and apparent oxide density are lower at this defect than it is in the surrounding surface. There is also surface debris associated with the defect.

Figure 2 shows cross-section SEM images of the unsealed oxide. Figure 2A shows defects through the full thickness of the layer. These appear to be partially filled or possibly empty. Figure 2B shows a single cavity in more detail. The oxide film surface was to the right hand side of the field of view. In this case, the cavity is partly filled by an intermetallic particle that has partially corroded during anodising. Disruption of the pore structure is evident, particularly between the alloy substrate and the particle, but this does not appear to affect the oxide density significantly.

By comparison with the SAA as-oxidised surface, sealing resulted in a much coarser, uniform surface morphology that completely obscured the underlying pore structure, as shown in Figure 3.

TEM Observations

Away from the intermetallic particles, the pore structure of the oxide was very regular, from the barrier layer through the layer thickness

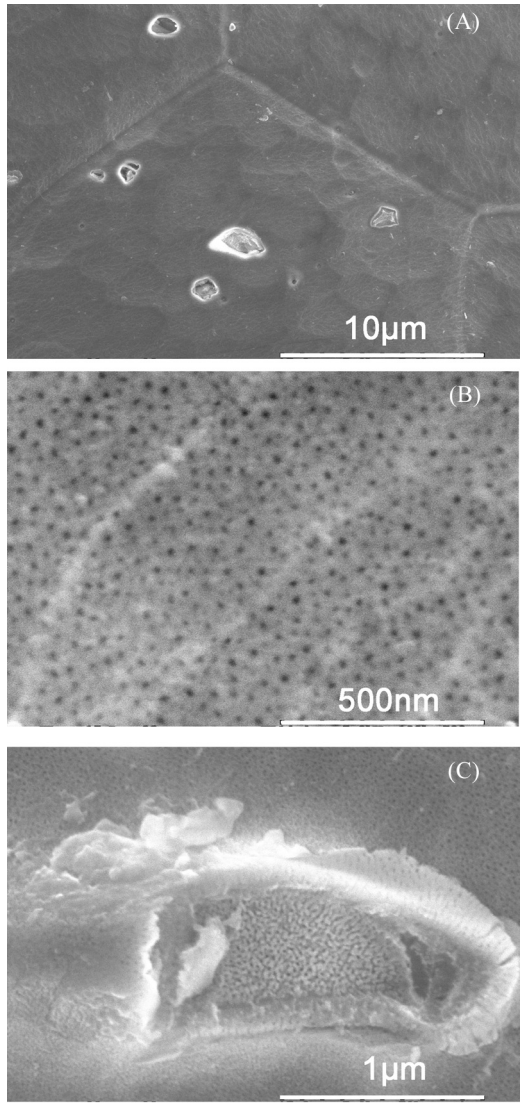

FIGURE 1 SEM images showing the surface of the unsealed oxide. 1A includes part of four grains in the underlying alloy. 1B shows detail of the pore structure. 1C shows detail of a surface defect.

and to the surface, as shown in Figure 4. Figure 4A shows the outer surface of the oxide while Figure 4B shows the bulk pore structure approximately in the middle of the layer. Comparison with the SEM

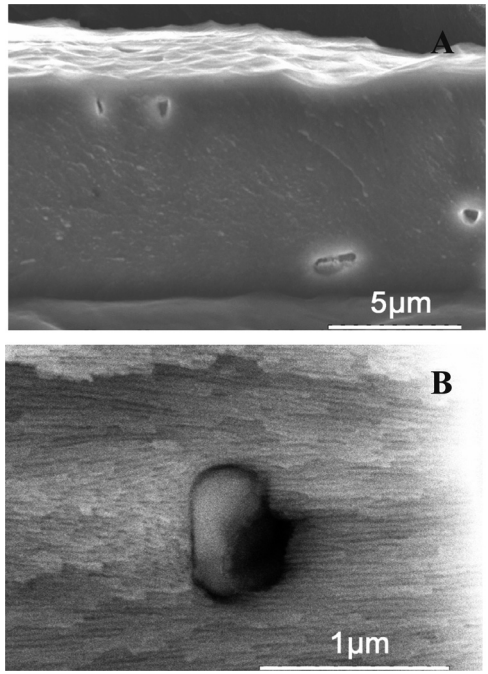

FIGURE 2 SEM images showing detail of the oxide cross section. 2A shows the full thickness of the oxide. 2B, rotated 90 degrees with respect to 2A, shows a cavity containing a partially dissolved intermetallic particle.

images in Figure 1B shows that there is partial closing of the pores at the outer surface.

Figure 5 shows an intermetallic particle that has been trapped in the layer. From the bright-field image of Figure 5A, it is clear that the particle has been partially dissolved from the surface that was first to be exposed to the electrolyte. Above the residual particle material, there is a volume of oxide showing lower density than the surrounding oxide. This volume probably defines the morphology of the original particle which has been significantly corroded during anodising [8]. A small volume of modified oxide, here protruding from the upper left surface of the cavity, was observed on several trapped particle cavities.

The distance between the particle and the underlying alloy is approximately 1 μm. The pore structure within this volume has been disrupted significantly by the presence of the particle which has, to an extent, protected the underlying alloy from the anodising process. As a result, a pyramid of alloy has been left on the alloy surface.

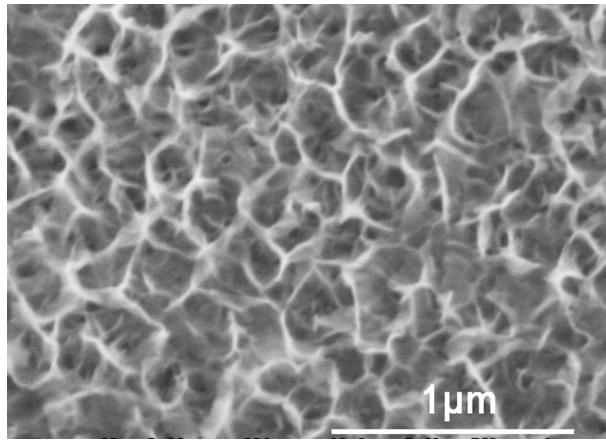

FIGURE 3 SEM images showing the surface of the oxide after sealing.

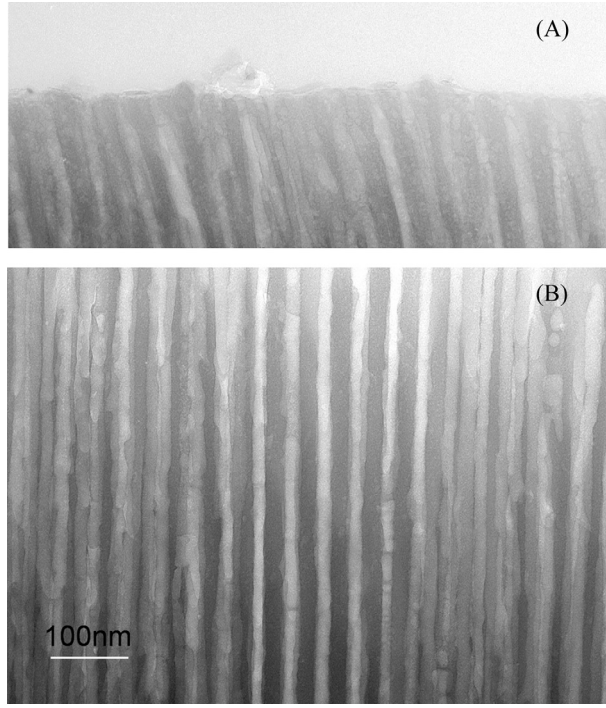

FIGURE 4 TEM sections showing the pore structure of the unsealed oxide. 4A shows the surface and 4B the mid-thickness structure of the oxide.

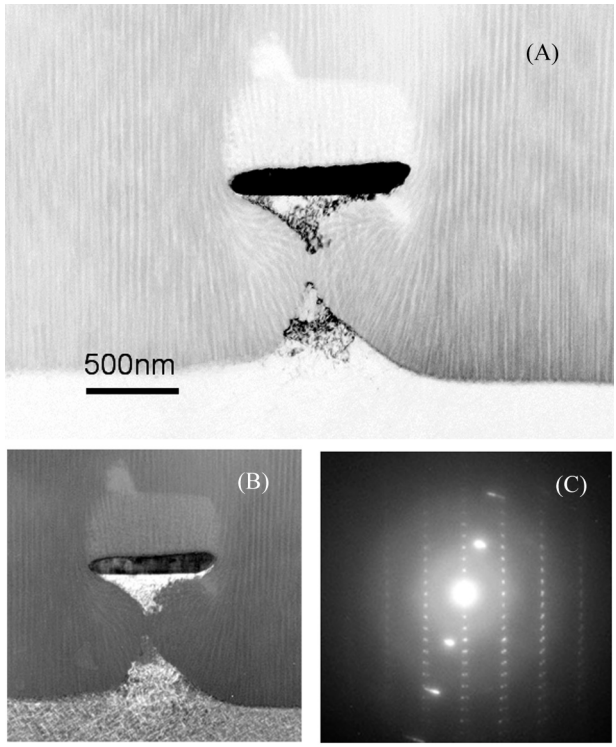

FIGURE 5 TEM observation of a partially corroded intermetallic particle trapped in the oxide, modified local alloy surface, retained aluminium and disrupted pore structure. 5A shows a bright field image. 5B shows a dark field image formed by a reflection from the aluminium alloy. The inset diffraction pattern shows two matrix reflections and a zone axis diffraction pattern from the particle.

Furthermore, some of the alloy has been retained in the oxide directly underneath the particle. This is shown more clearly by the dark field image of Figure 5B, which was produced from an aluminium 111-type reflection. Within the alloy, contrast from the β″ hardening phase gives a fine texture in the matrix. The material in the pyramid shows the same contrast, confirming that it is unmodified matrix having the same orientation as the underlying matrix and containing β″ precipitates. The selected area diffraction pattern from the residual particle, including a systematic row of reflections from the trapped aluminium matrix, shown in Figure 5C, is consistent with the hexagonal structure expected for the Fe-rich variant of the α–Al(Fe,Mn)Si phase [15].

The overall composition of the residual α–Al(Fe,Mn)Si, with negligible Mn content, is confirmed by energy dispersive (EDS) x-ray analysis shown in Figure 6A. The Cu peak is an artefact due to secondary excitation of material in the sample holder and the column of the electron microscope. Figure 6B shows the EDS spectrum obtained from the adjacent low density material in the cavity. This shows that that the cavity has retained some of the constituent elements of the particle. Tilting of the sample did not produce any diffraction contrast in the cavity oxide, confirming that it was amorphous. Figure 6C shows the EDS spectrum obtained from the adjacent regular oxide. No significant enrichment of alloying or impurity elements from the alloy was found in the bulk of the anodic oxide. A significant level of S, roughly 5 at%, has been retained in the alloy. The relative strength of the O and Al peaks in Figures 6B and 6C shows that the Fe and Si are probably present in the form of oxide.

Several similar examples of trapped intermetallic particles were observed. In some cases no residual intermetallic particle was observed, but Fe and Si were detected at positions where the oxide pore structure was disrupted. The scale of the cavities in the oxide is comparable with the size of the intermetallic particles observed in the unoxidised matrix.

The sealed sample showed a modified pore structure through the full thickness of the layer, extending down to the barrier layer. Figure 7 shows a cross-section view of the structure at the surface, A, mid-depth, B, and barrier layer, C. Within the pores, a fine network of bridging ligaments closes the pores partially. At the very surface, a layer of low density material with irregular morphology is present. This corresponds well with the coarse surface structure observed in the SEM image of Figure 3.

SIMS Analysis

The intensity of the Al peak was almost constant in the surface oxide then increased and became constant in the matrix. The change in signal is partly due to the change in stoichiometry from oxide to metal and partly due to the higher sputtering rate in the alloy. Figure 8 shows the elemental depth profile obtained in the first SIMS analysis where the transition from oxide took place at a depth of 10–11 μm. Figure 8A shows the distribution of H and S. These profiles are qualitative as we lacked S and H standards. However, the S profile has been normalized using the S concentration measured in the oxide by EDS. The level of the former is highest at the surface of the oxide and falls gradually towards the barrier, probably reflecting the slow

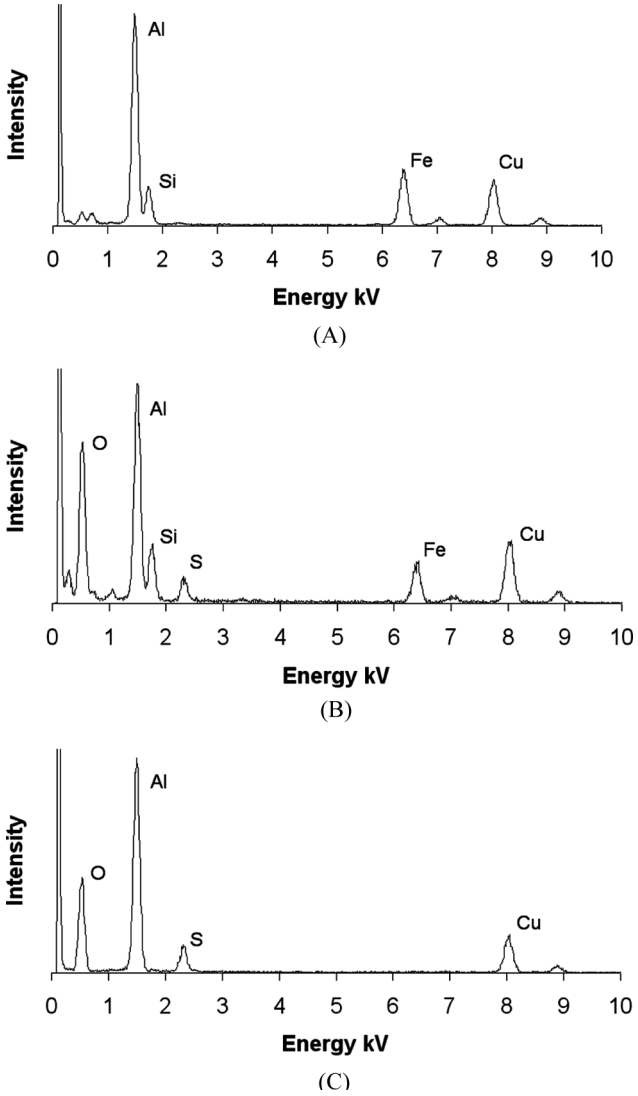

FIGURE 6 EDS analysis of the cavity of Figure 5. 6A is from the residual particle material, 6B the low density oxide in the cavity, and 6C the adjacent bulk oxide.

hydration of the inside of the pores. The latter, derived from the electrolyte, rises slightly through the thickness of the oxide until the barrier is reached and falls rapidly as the profile moves into the alloy.

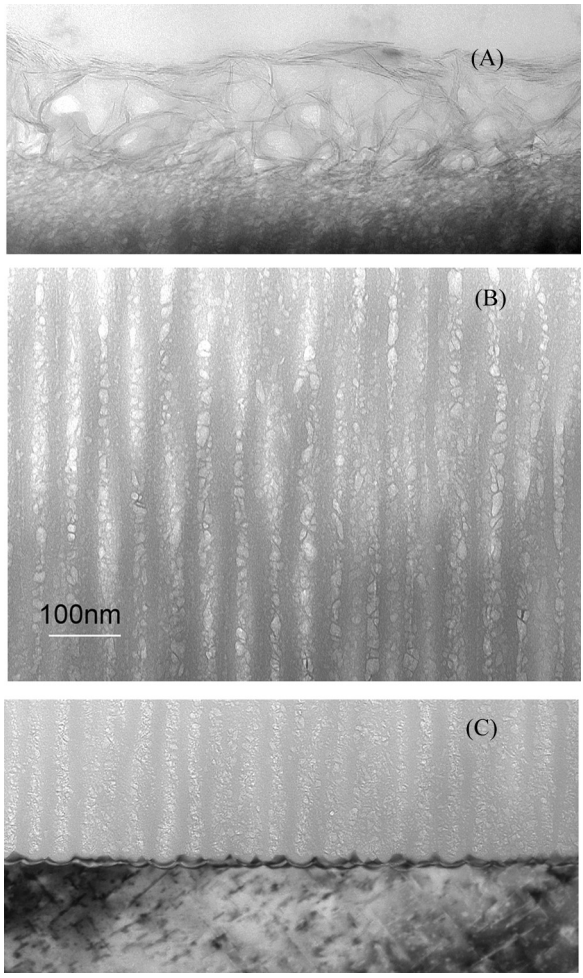

FIGURE 7 TEM sections showing the pore structure after sealing. 7A shows the surface. 7B shows the mid-thickness structure of the oxide. 7C includes the barrier layer.

Figure 8B shows the depth distribution of three of the major alloying elements in the alloy and calcium. The variations in Fe demonstrate that the area of the alumina layer analysed contained three Fe-particles in the size range 0.5–3 μm within the first 5 μm above the alloy. Si from the particles is largely masked by the high background level of this element, derived from the β″ hardening phase and residual solid solution in the matrix, although some correlation is

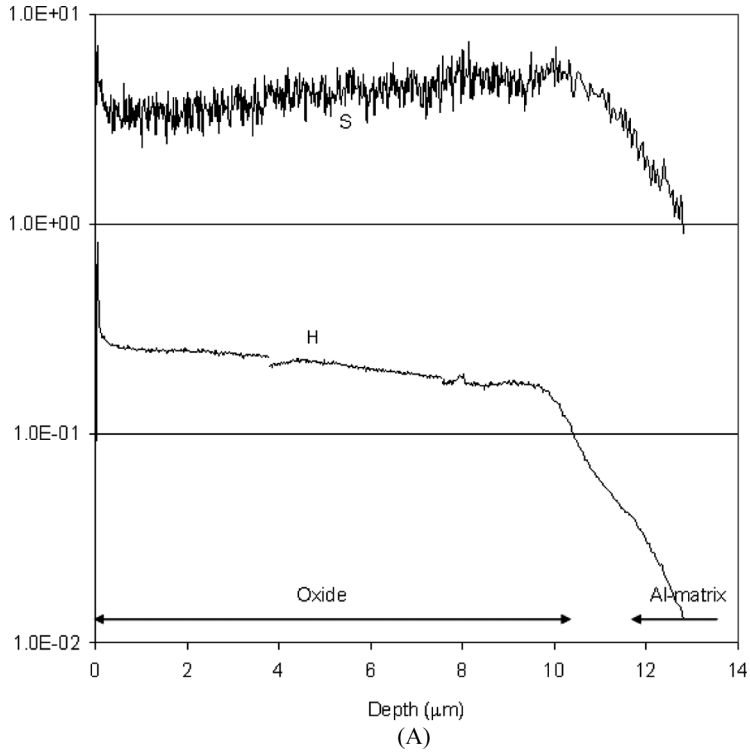

FIGURE 8 SIMS concentration profiles from the first position in the unsealed sample. 8A shows the corrected depth concentrations for H and S, elements which are derived from the electrolyte. 8B shows the depth concentrations for the main alloying elements, Mg, Si, and Fe, plus Ca.

present in the Si signal at the position of the intermetallic particle nearest to the alloy. The Mg level is fairly constant within the alloy and rises at the interface to the matrix level.

Figure 9 shows the element depth profiles obtained for Mg, Si, Fe, and Mn for the second SIMS analysis, which was performed at a separate position on the surface of the same sample. The results for this analysis were roughly similar to those at the first position. The Fe profile suggests that two intermetallic particles were present in the analysed volume. It also does not show the plateau of increased Fe within a couple of microns of the oxide surface that was present in the first profile. The Mn profile does not show any corresponding variations, supporting the TEM observation that the intermetallic particles are Fe-rich and that the Mn content in the oxide represents the direct

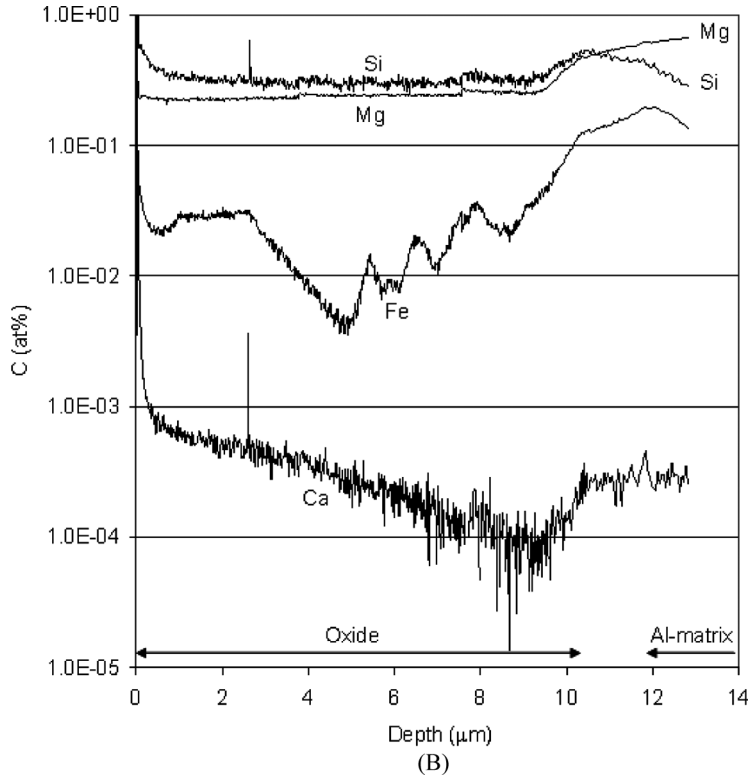

FIGURE 8 Continued.

incorporation of this element from solid solution. The transition from metal matrix to oxide gives, as expected, a reduction in the concentration of the Si, Mg, Mn, and Fe, while impurity elements like H and Ca have a concentration profile indicating that the element diffuses into the metal during anodising.

DISCUSSION

Under the given anodising conditions, intermetallic particles are partially retained within the oxide. Oxidation of the particles is comparatively rapid when they are initially exposed to the electrolyte and slows, but probably does not stop, once they are enclosed within the oxide. The continued dissolution of the particles is supported by the SIMS depth profiles that show corresponding fluctuations in Fe concentrations within a few micrometers of the metal oxide interface. This

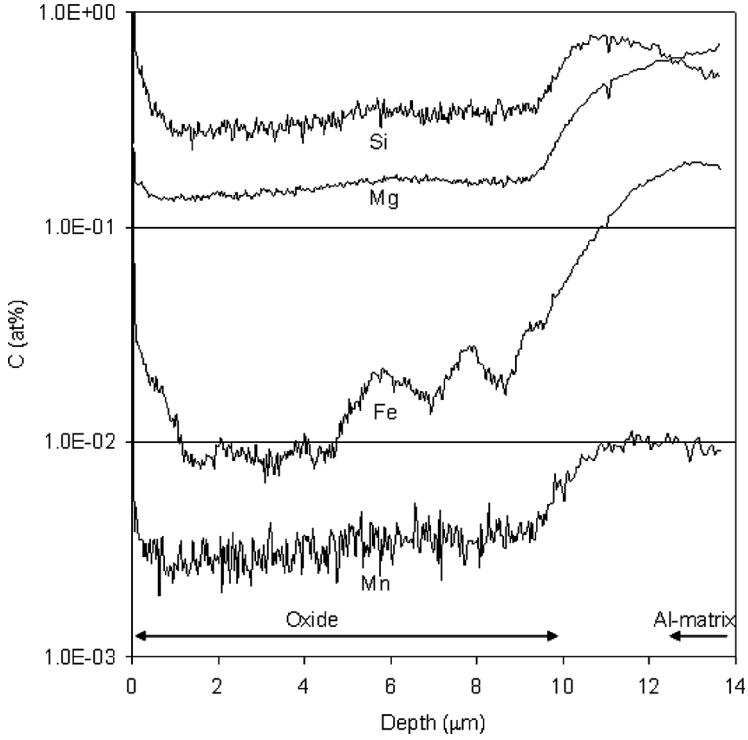

FIGURE 9 SIMS concentration profiles from the second position in the unsealed sample showing the four main alloying elements.

is similar to the behaviour observed for intermetallic particles in other aluminium alloy systems [8–12].

The retained particles influence the local pore morphology. The pore diameters behind the particles is not significantly altered. However, access of the electrolyte to the alloy is less direct, reducing the local rate of oxidation of the alloy. This leads to the presence of conical defects on the alloy surface. Similar substrate morphology is evident in the work of Shimizu *et al.* due to the influence of an Al_6Fe particle [8]. A new observation reported here is that the obstruction of the pore structure by the particle cavity provides a mechanism for the retention of unmodified matrix alloy in the oxide under the particle cavities.

The particle cavities provide defects and local enrichment of alloying elements in the oxide. When the observed density of cavities may have a significant effect on applications, the use of a more aggressive electrolyte or variation of the anodisation parameters could probably be

used to control the particles by increasing their dissolution rate, as suggested by Mukhopadhyay and Sharma [10].

Sealing results in partial closure along the full length of the pores which can clearly improve the corrosion resistance of the surface by reducing the access of corrosive agents such as moisture and chloride ions to the bulk of the oxide.

SIMS profiles for the unsealed sample were discontinued as soon as it was judged that the matrix had been exposed. This makes it difficult to interpret the behaviour of the profiles on moving into the alloy matrix with complete confidence, particularly with respect to enrichment of elements under the barrier layer. In the Fe profile of Figure 8B, it is possible that one or more intermetallic particles were exposed at the position of the oxide alloy interface. This profile and that of Figure 9 show a possible enrichment around the position of the barrier layer. Considering other elements, Si seems to be enriched at the interface, falling on moving into the alloy. S is slightly enriched at the interface, although this element is derived from the electrolyte. By comparison, Mg, Ca, and Mn levels increase to a constant level on going through the barrier layer. Acording to the Gibbs' free energy arguments for binary systems referred to above [4–6], enrichment of the alloy under the barrier layer is expected to an increasing degree for Si, Mn, and Fe. For Ca, a marginal enrichment is predicted and no enrichment is predicted for Mg. With the exception of Mn, whose level in this alloy is considerably lower than that considered in the earlier binary alloy studies, the observations suggest that, allowing for the fact that the levels of elements vary significantly and may be present as precipitates as well as in being in solid solution, the alloying elements in this alloy may behave in a manner that is roughly consistent with the principles described in [4]. While this correlation is preliminary, the observations indicate that SIMS can be a powerful technique for the study of these effects when changes in sputtering rate on going from oxide to alloy are taken into account. SIMS may be particularly useful in studies of thicker films where techniques such as Rutherford Backscattering may not be appropriate and for industrial systems where a large number of alloying and impurity elements are generally present. SIMS also has the advantage of analysing bulk that has not been in contact with chemicals during specimen preparation, an operation that may change the local composition.

CONCLUSIONS

During DC anodising of AA6061 alloy under SAA conditions, intermetallic α–Al(Fe,Mn)Si particles become incorporated in the growing ano-

dic film. The particles are attacked immediately on exposure to the electrolyte, as the oxide alloy interface advances, and probably continue to be dissolved at a slower rate as the film grows.

The pore structure is disrupted around the particle, resulting in a reduced local anodising rate. This leads to pyramidal defects forming on the alloy surface and unmodified aluminium alloy being incorporated in the anodic layer on the alloy side of the particle cavities.

The simple sealing process used here leads to the presence of a low density surface layer. In the bulk of the oxide, sealing forms a fine network of bridges that at least partially close the pores throughout the full thickness of the film.

Besides giving information about the impurity content of the bulk oxide, preliminary interpretation of the SIMS data indicates enrichment of elements in the region of the barrier layer that would be predicted for anodisation of binary alloys, and this merits further investigation.

ACKNOWLEDGMENTS

The authors would like to acknowledge the financial support of the Norwegian Research Council. They would also like to thank Hans Odelius and Ulf Södervall for expert assistance in performing the SIMS experiments.

REFERENCES

[1] Bjørgum, A., Lapique, F., Walmsley, J., and Redford, K., *Int. J. Adhesives* **23** (5), 401–412 (2003).
[2] Tsagararaki-Kaplanogou, I., Theohari, S., Dimogerontakis, T., Wang, Y. M., Kuo, H. H., and Kia, S., *Surface and Coatings Technology* **200**, 2634–2641 (2006).
[3] Habazaki, H., Shumizi, K., Skeldon, P., Thompson, G. E., and Wood, G. C., *Phil. Mag. B* **73** (3), 445–460 (1996).
[4] Habazaki, H., Shumizi, K., Skeldon, P., Thompson, G. E., Wood, G. C., and Zhou, X., *Trans IMF* **75** (1), 18–23 (1997).
[5] Habazaki, H., Shumizi, K., Skeldon, P., Thompson G. E., Wood, G. C., and Zhou, X., *Corrosion Science* **39** (4), 731–737 (1997).
[6] Thompson, G. E., Habazaki, H., Shimizu, K., Zhou, X., and Wood, G. C., *Aircraft Engineering and Aerospace Technology* **71** (3), 228–238 (1999).
[7] Hazabaki, H., Konno, H., Shimizu, K., Nagata, S., Skeldon, P., and Thompson, G. E., *Corrosion Science* **46**, 2041–2053 (2004).
[8] Shimizu, K., Brown, G. M., Kobayashi, K., Skelden, P., Thompson, G. E., and Wood, G. C., *Aluminium Surface Science and Technology*, (1997) pp. 189–194.
[9] Shimizu, K., Thompson, G. E., Wood, G. C., and Kobayashi, K., *Journal of Materials Science Letters* **10**, 709–711 (1991).
[10] Mukhopadhyay, K. A. and Sharma, K. A., *Surface and Coatings Technology* **92**, 212–220 (1997).

[11] Fratila-Apachitei, L. E., Tichelaar, F. D., Thompson, G. E., Terryn, H., Skeldon, P., Duszczyk, J., and Katgerman, K. A., *Electrochemica Acta* **49**, 3169–3177 (2004).
[12] Shimizu, K., Kobayashi, K., Thompson, G. E., Skeldon, P., and Wood, G. C., *Corrosion Sci.*, **39** (2), 281–284 (1997).
[13] Shimizu, K., Kobayashi, K., Thompson, G. E., Wood, G. C., and Skeldon, P., *Phil. Trans. Roy. Soc.* **354**, 213–235 (1996).
[14] Simensen, C. J. and Södervall, U., *Surf. Interf. Anal. 30*, 309–314 (2000).
[15] Tibballs, J. E. and Simensen, C. J., *J. Mater. Sci.* **36**, 937–941 (2001).